

Numerical Simulation of Orthogonal Cutting using the Material Point Method

John A. Nairn

Wood Science and Engineering, Oregon State University, Corvallis, OR 97330, USA

Tel: +1-541-737-4265

Fax: +1-541-737-3385

Email: John.Nairn@oregonstate.edu

Abstract

A material point method simulation of orthogonal cutting that can simulate cutting into steady-state chip curling is described. The modeling used ductile fracture mechanics using cohesive zone in the cutting path. Robust simulations required a new mechanism to damp kinetic energy artifacts associated with dynamic crack propagation. The simulations displayed two regimes — crack-tip touching, where the tool reaches the crack tip, and plastic bending, where the tool is separated from the crack tip by a gap. The simulations were compared to analytical models that were revised to account for rubbing forces and hardening laws.

Key words: A. Cutting, B. Material Point Method, C. Computational Mechanics, D. Cohesive Zones

1. Introduction

Several recent papers advocate modeling of orthogonal cutting as a ductile fracture mechanics problem for a crack propagating in the direction of the tool tip [1, 2, 3, 4, 5, 6, 7]. Some analytical modeling [1, 6] and experiments [4, 5, 8] show the fracture mechanics view can help interpret experiments and explain some problems of classic cutting models based solely on plasticity and friction [1, 2]. A suggestion of this new approach is that cutting experiments can be used to measure the toughness of ductile materials. The concept is that extrapolation of cutting forces to zero depth of cut should have non-zero intercept equal to the material's fracture toughness. The challenge is to devise the best experimental methods for getting reliable extrapolations in the presence or large amounts of work due to plasticity and friction. Recommendation of such experimental protocols should be guided by modeling. The current analytical modeling has been limited to basic material properties, simple yielding models (such as elastic-plastic), and simple frictional contact. This paper's goal is to develop a numerical model for orthogonal cutting with the potential to handle more realistic material properties (such as large-strain constitutive laws), arbitrary plasticity and contact laws, and more realistic specimen geometries and boundary conditions.

The numerical modeling of orthogonal cutting through to steady-state chip curling and wrapping involves large strains (close to 100% shear strains are seen in calculations), large displacements and rotations, dynamic contact both between the tool and the cut material and between layers of a curling chip, and evolution of an explicit crack. The finite element method (FEM) has been used for orthogonal cutting (e.g., [9]). In general, prior FEM models have assumed the process is dominated by plasticity and friction and ignored crack propagation in the path of the tool. Most have been for small amounts of

chip formation, rather than complete chip formation into the steady-state cutting regime. A drawback of many FEM models is severe mesh distortion requiring adaptive remeshing [9]. Furthermore, FEM plasticity and friction models cannot model significant tool movement without addition of a separation criterion (e.g., stress or strain limits) [1]. Such *ad hoc* criteria may not provide a rigorous fracture mechanics simulation of cutting.

A alternative numerical method, called the material point method (MPM) [10, 11], seems well suited to simulations of orthogonal cutting problems. It can handle large strains and deformations without remeshing, dynamically model all contact situations [12, 13], and implement explicit cracks [14, 15] for ductile fracture mechanics. This paper presents an MPM model of orthogonal cutting through to steady-state cutting with chip curling. The simulations worked well, but required development of a new MPM damping scheme, called “PIC Damping,” that appears especially effective at damping vibrations caused by kinetic energy released in dynamic crack propagation. The simulations were verified by comparison to analytical models, but the models had to be modified to account for “rubbing” forces on the bottom of the tool and to handle elastic-plastic materials with linear hardening. The cutting simulations displayed two cutting regimes — chip shearing, where the tool tip touches the crack tip, and plastic bending, where the chip is bent but the tool tip is displaced from the crack tip. The shearing occurred for thin cuts followed by a sudden transition to plastic bending with a drop in cutting forces for thicker cuts. The simulations could handle both regimes and the transition between the two regimes. The explicit crack propagation was handled by using a cohesive zone model along the cutting path.

2. Numerical Methods

The material point method (MPM) discretizes the object into particles and uses a background grid for solution of the momentum equation [10]. The geometry and discretization for the MPM model are shown schematically in Fig. 1. The simulations varied the depth of cut (h). The specimen’s width, base depth, and pre-existing crack length were scaled to depth of cut as wh , bh , and ah , respectively, using scaling factors w , b , and a . The width and crack length factors were set to $w = 30$ and $a = 18$, which provided enough cutting length to achieve steady state cutting as well as complete chipping curling. The base factor was set to $b = 3$ (as explained below). The tool rake angle (α) was varied while the clearance angle was kept constant at $\theta = 5^\circ$. The specimen’s entire bottom edge was held at zero displacement in both the x and y directions. The inset shows the background grid and MPM particles near the initial notch tip (at lower resolution than used in simulations). The specimen filled the grid with four particles per cell. The tool also used four particle per cell, but sheared those particles to conform to the tool shape. This inset shows particles drawn at 60% of their size. The actual MPM particles, as quadrilateral regions, completely filled space in both the specimen and the tool.

Because cutting simulations result in large deformations and large-scale rotations, it was crucial to use a hyper-elastic, plastic material model for the specimen [16]. The elastic response of the isotropic material was modeled as a neo-Hookean material with elastic strain energy given by:

$$W = \frac{K}{2} \left(\frac{1}{2} (J_e^2 - 1) - \ln J_e \right) + \frac{G}{2} \left(\text{Tr} \overline{\mathbf{B}}_e - 3 \right) \quad (1)$$

Here $J_e = \det \mathbf{F}_e$ is determinant of the elastic deformation gradient, $\overline{\mathbf{B}}_e = \overline{\mathbf{F}}_e \overline{\mathbf{F}}_e^T$ is the deviatoric part of the left Cauchy-Green strain tensor, $\overline{\mathbf{F}}_e = \mathbf{F}_e / J_e^{1/3}$ is the deviatoric part of the elastic deformation

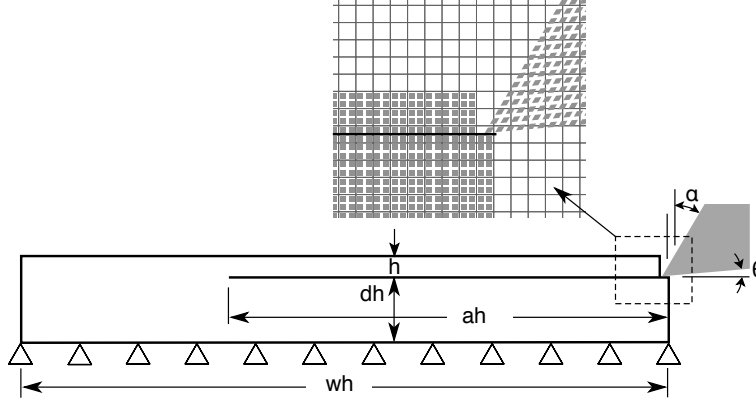


Figure 1: A schematic drawing of the numerical model for orthogonal cutting to a depth of cut h with initial crack length ah , base depth dh , and total width wh . The tool has rake angle α and clearance angle θ . The inset shows MPM background grid and discretization into material points in the cut material and the rigid tool. All simulations used more particles, or higher resolution, then depicted in the inset.

gradient, and K and G are the low-strain bulk and shear moduli of the material. The plastic response was modeled by yielding when the magnitude of the deviatoric stress reaches

$$\|s\| = \sqrt{\frac{2}{3}} f(\epsilon) \quad (2)$$

where $f(\epsilon)$ is any hardening law that depends on cumulative plastic strain ϵ found by integrating $d\epsilon = \sqrt{2/3} \|d\epsilon_p\|$ where $d\epsilon_p$ is the incremental plastic strain tensor. Any hardening law can be used, but all simulations here compared to analytical models and thus were limited to linear hardening with $f(\epsilon) = \sigma_{y0} + E_p \epsilon$, where σ_{y0} is the initial yield stress and E_p is the plastic modulus. Material properties were set by selecting a tangent modulus E_T as the slope of a tensile stress-strain curve in the plastic region, from which plastic modulus is $E_p = EE_T / (E - E_T)$ where E is the low-strain elastic modulus. The plastic response was implemented using return mapping methods [17].

Crack propagation was modeling using the CRAMP algorithm for addition of explicit cracks to MPM simulations [14]. Because it was difficult to control crack propagation and direction from the complex and large plastic deformation processes near the crack tip, the crack propagation was modeled using cohesive zones. In brief, an explicit crack of length ah was inserted at the start of the calculations. To help in starting the cutting process, a distance $2h$ at the beginning of the crack was inserted as a traction-free crack. The remaining length of the crack incorporated cohesive traction laws as described for MPM simulations by Nairn [15]. Most simulations used a cubic traction law:

$$\sigma = \frac{27}{4} \sigma_c \frac{\delta}{\delta_c} \left(1 - \frac{\delta}{\delta_c}\right)^2 \quad (3)$$

where σ_c is the cohesive stress and δ_c is the critical crack opening displacement [18]. The area under this law is the toughness $J_c = 9\sigma_c \delta_c / 16$. A simple approach to mixed-mode loading is a decoupled failure criterion [19]:

$$1 = \frac{J_I(\delta_n)}{J_{Ic}} + \frac{J_{II}(\delta_t)}{J_{IIc}} \quad (4)$$

where $J_I(\delta_n)$ and $J_{II}(\delta_t)$ are areas under the mode I and II cohesive laws up to normal (δ_n) and tangential (δ_t) crack opening displacements and J_{Ic} and J_{IIc} are toughnesses in pure mode I and II. To minimize the number of simulation parameters, all simulations here used the same cohesive laws in mode I and II ($J_{Ic} = J_{IIc} = J_c$ and $\sigma_{Ic} = \sigma_{IIc} = \sigma_c$); *i.e.*, failure occurs when total energy release rate $J_c = J_I(\delta_n) + J_{II}(\delta_t)$. The fraction of mode I energy released ($J_I(\delta_n)/J_c$) was output during crack growth to evaluate the mode-mixity of the cutting process.

The tool was modeled as a rigid material. The particle centers were aligned to conform to the tool's rake and clearance angles and the initial particle domains (squares) were sheared to parallelograms to have domain edges exactly match the tool edges (see Fig. 1). Although aligning particle centers always helped the calculations, shearing the domains only influences the results when using shape function methods that account for domain deformation (*e.g.*, convected particle domain integration or CPDI [20]). All calculations here using uniform, generalized interpolation methods (or uGIMP [11]) where the integration domain remains a square, but translates with the particles; uGIMP was used for all simulations because it was more efficient and accounting for domain shearing (with CPDI) had very little effect.

The rigid particles in the tool ignored the crack planes used by the CRAMP algorithm [14], which allowed the tool to interact with both the top and bottom surfaces of the crack through contact mechanics. In other words, this special material could be inside a crack and serve to wedge open the crack including touching the crack tip when material properties allowed it. The contact was modeled using Coulomb friction using MPM multimaterial contact methods [12]. Recent work on contact methods has emphasized the importance of accurately calculating the contact normals [13, 21]. This issue could be handled rigorously for these cutting simulations because all contact normals could be predetermined. The normal (from cut material into the tool) on the tool's top surface was set to $\hat{n} = (\sin \alpha, -\cos \alpha)$ and on the bottom surface was set to $\hat{n} = (0, 1)$.

2.1. PIC Damping

The most important MPM change that led to robust and stable simulations for a wide variety of specimen geometries, material properties, and cohesive law properties was to introduce a new method for updating particle velocity and position. The MPM time step solves the momentum equation on the background grid or

$$\mathbf{p}_i^{(n+1)} = \mathbf{p}_i^{(n)} + m_i^{(n)} \mathbf{a}_i^{(n)} \Delta t \quad (5)$$

Here subscript i indicates a nodal value, subscripts (n) and $(n+1)$ denote time step n and the updated results, \mathbf{p} is momentum, \mathbf{a} is acceleration, and m is mass. Once the grid update is done, these results are used to update particle velocity and position. The standard methods used by MPM codes is a FLIP method (for Full Lagrangian Implicit Particle [22]) where particle velocity, \mathbf{v} , is updated using the grid acceleration:

$$\mathbf{v}_{p,FLIP}^{(n+1)} = \mathbf{v}_p^{(n)} + \mathbf{a}_{g \rightarrow p}^{(n)} \Delta t \quad \text{where} \quad \mathbf{a}_{g \rightarrow p}^{(n)} = \sum_i \mathbf{a}_i^{(n)} S_{ip}^{(n)} \quad (6)$$

Here subscript p indicates a particle quantity and subscript $g \rightarrow p$ indicates extrapolation of a grid result to the particle location using the MPM shape function (S_{ip}) [11]. An alternative update scheme used in particle methods is the PIC method (for Particle In Cell [23]) that extrapolates grid velocity directly to the particle:

$$\mathbf{v}_{p,PIC}^{(n+1)} = \mathbf{v}_{g \rightarrow p}^{(n+1)} = \mathbf{v}_{g \rightarrow p}^{(n)} + \mathbf{a}_{g \rightarrow p}^{(n)} \Delta t \quad \text{where} \quad \mathbf{v}_{g \rightarrow p}^{(n)} = \sum_i \frac{\mathbf{p}_i^{(n)}}{m_i^{(n)}} S_{ip}^{(n)} \quad (7)$$

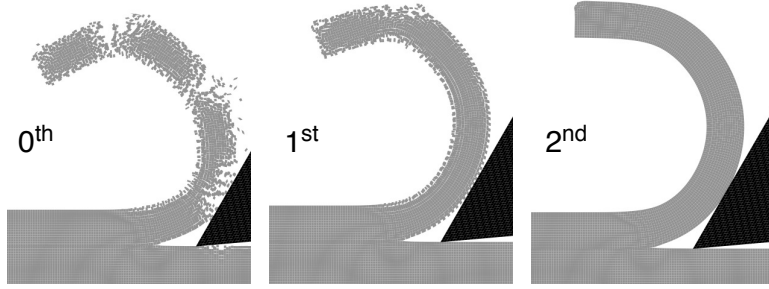


Figure 2: Simulation of orthogonal cutting using 100% PIC update for velocity by various updates for position. The 0th update used Eq. (9), which is the standard MPM update when using FLIP update for velocity. The 1st and 2nd updates used Eq. (10) to first or second order in Δt , respectively.

The FLIP method was preferred because PIC can cause numerical diffusion resulting in higher viscosity and heat conduction than expected [22]. But, Stomakhin *et al.* [24] suggests that MPM simulations can be improved by combining FLIP and PIC simulations and this suggestion led to significant improvement in cutting simulations.

But two questions remained — why does addition of PIC help and is it reasonable to include it in MPM simulations? My proposal is that use of PIC in MPM simulations is better described as a new form of artificial damping applied to the preferred FLIP methods. This new form of damping seems to be particularly effective for simulations involving crack propagation. The numerical diffusion that is a concern for fluid dynamics modeling [22] may actually be a benefit to crack propagation modeling where the numerical diffusion dampens kinetic energy caused by increments in crack growth. In real materials, energy released by crack growth is absorbed by crack tip processes. But, in computational mechanics, dynamic crack propagation injects kinetic energy into the system that is not absorbed by standard material models. The addition of PIC damping seems to provide an effective damping mechanism for that unrealistic kinetic energy. A new FLIP velocity update with PIC damping can be written as

$$\mathbf{v}_p^{(n+1)} = \mathbf{v}_p^{(n)} + (\mathbf{a}_{g \rightarrow p}^{(n)} - \alpha_{PIC}(\mathbf{v}_p^{(n)} - \mathbf{v}_{g \rightarrow p}^{(n)}))\Delta t \quad (8)$$

where $\alpha_{PIC} = (1 - \beta)/\Delta t$ is a PIC damping coefficient. The term β varies from 1, which gives a pure FLIP velocity update, to 0, which gives a pure PIC velocity update (*cf.* Eqs. (6) and (7)). This general equation has the standard form for damping where the acceleration is reduced by a term proportional to velocity. A unique feature of MPM exploited here is that there are two velocities — current particle velocity ($\mathbf{v}_p^{(n)}$) and the velocity extrapolated from the grid to the particle ($\mathbf{v}_{g \rightarrow p}^{(n)}$). In well behaved simulations, these two velocities remain close such that the standard update proceeds by FLIP methods. When MPM encounters noise (such as kinetic energy injected into the system by propagating an existing crack), that noise is sometimes reflected in velocity variations within a background cell that can cause differences between these two velocities. PIC damping can be viewed as damping out such local velocity “errors.”

Another advantage of viewing PIC as a damping mechanism is that it provides guidance for how to modify the position update as well. All current MPM codes use first order FLIP position update of

$$\mathbf{x}_p^{(n+1)} = \mathbf{x}_p^{(n)} + \mathbf{v}_{g \rightarrow p}^{(n+1)}\Delta t \quad (9)$$

When Stomakhin *et al.* [24] added partial PIC updates, they did not change this position update, but

they only used 5-10% PIC and may not have needed a change. When using more PIC damping, it is vital to modify the position update as well. By integrating $\mathbf{v}_{g \rightarrow p}^{(n+1)} dt$ from 0 to Δt using the midpoint rule, a general second order FLIP position update is derived as:

$$\mathbf{x}_p^{(n+1)} = \mathbf{x}_p^{(n)} + \mathbf{v}_{g \rightarrow p}^{(n+1)} \Delta t - \frac{1}{2} \left(\mathbf{a}_{g \rightarrow p}^{(n)} + \alpha_{PIC} (\mathbf{v}_p^{(n)} - \mathbf{v}_{g \rightarrow p}^{(n)}) \right) (\Delta t)^2 \quad (10)$$

Figure 2 shows the results of cutting simulations after the onset of chip curling when using full PIC damping ($\beta = 0$) but varying the position update method. The three position updates were the standard MPM position (0^{th} order or Eq. (9)), the modified update in Eq. (10) to 1^{st} order (which includes the α_{PIC} term but not the $\mathbf{a}_{g \rightarrow p}^{(n)}$), and the full 2^{nd} order Eq. (10). This figure plots glyphs at each material point that were deformed from their initial square to a parallelogram defined by the deformation gradient on the particle. A good simulation should fill space with no gaps. Clearly, when PIC damping is used to alter the velocity update, the position update must change as well. This fact is shown by the very poor results when using 0^{th} order. When PIC damping is used, a first order update is not enough. This observation is illustrated by the 1^{st} order diagram in Fig. 2. By this method, the particles near the edges, which are the particles with the most deformation, do not update well. All issues are fixed by the 2^{nd} order update where the deformed glyphs reveal highly accurate tracking of particle deformations including those that are highly deformed on the edges of the curling chip (see Fig. 2).

2.2. Steady State Cutting Simulations

A goal of the simulations was to achieve steady-state cutting with chip curling; all simulations used the open-source MPM software NairnMPM [25]. The cutting speed was set to 2 m/sec. Applying this speed at the start of the simulation, however, caused inertial effects. To minimize these effects, the tool speed was gradually increased from zero to 2 m/sec over the first 30% of the total simulation time. During this ramp phase, the simulations were damped using a variant of a Nose-Hoover thermostat [26, 27]. This thermostat adds damping in a feedback mechanism based on total kinetic energy. One change made from a prior MPM implementation [27] was to evaluate total kinetic energy from grid masses and velocities rather than particle masses and velocity. Like the PIC damping discussed above, the grid kinetic energy was less prone to velocity "errors" and gave more reliable damping. The feedback damping was turned off once the tool reached full speed. The PIC damping, however, was left on throughout the entire simulations and used $\beta = 0$.

The intent of the simulation was to model a thin cut off a bulk material. The first approach was to use silent boundary conditions that are meant to absorb stress waves and thereby mimic simulations of an infinite medium [28]. Unfortunately, these boundary conditions did not achieve their goal in the cutting geometry. Instead, both x and y displacements on the bottom were fixed, but such conditions require sufficient depth to avoid edge effects. Figure 3 shows average cutting force as a function of the depth, dh , between the cutting plane and the rigid boundary conditions. As long as $d \geq 3$, the forces were constant and thus all simulations used $d = 3$. To determine resolution required, the particle size was varied. Figure 3 shows average cutting force as a function of particle size for depth of cut of 0.9 mm. The cutting force continued to decline. As a compromise for simulation time and resolution, all simulations used 15 particles through the thickness of the chip, which corresponds to 60 μm particle when depth of cut is 0.9 mm.

Combining all simulation strategies, Fig. 4 shows horizontal, F_c , and vertical, F_t , force of the tool on the cut material. The forces were determined by summing the momentum changes imposed by the contact algorithm on the rigid tool [13]. The cut material had $K = 980$ MPa, $G = 376$ MPa, $\sigma_{y0} = 25$ MPa, $E_T = 100$ MPa, and density $\rho = 1$ g/cm³. The cubic cohesive law had $G_c = 2000$ J/m²,

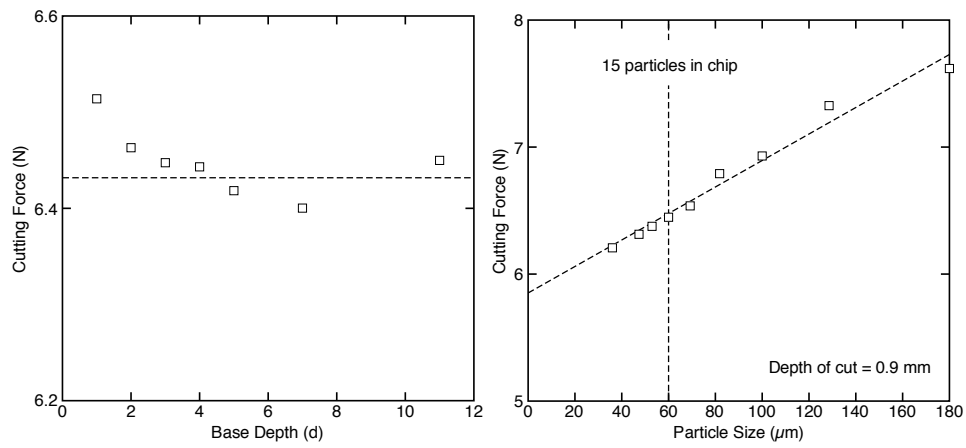


Figure 3: A. The cutting force as a function of depth of material below the cut plane. B. The cutting force as a function of particle size used in the MPM discretization. The depth of cut was 0.9 mm.

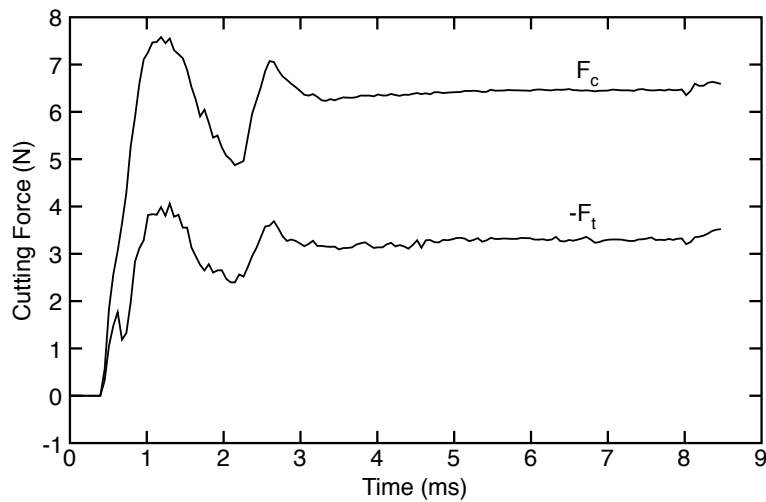


Figure 4: The cutting force, F_c and negative of the transverse force, $-F_t$, as a function of time for depth of cut of 0.9 mm and frictionless contact. All other material properties are listed in the text of the paper. The steady state forces were measured by averaging the forces in the constant regime (e.g., $t > 4$ ms).

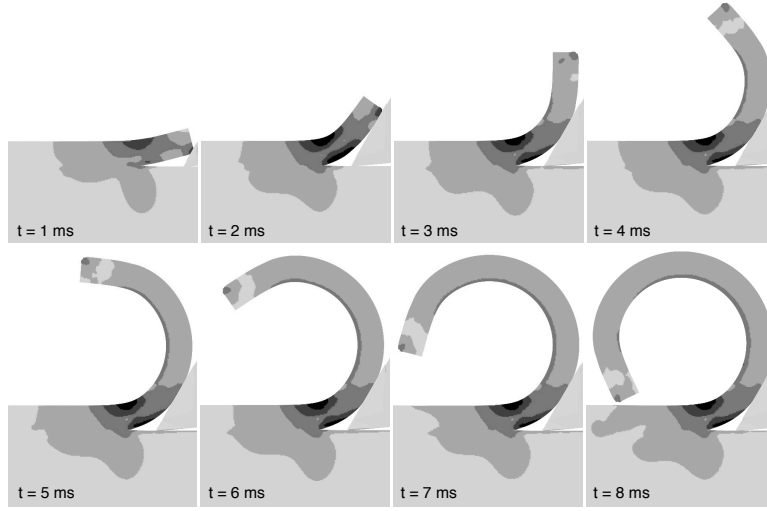


Figure 5: Snapshots of a cutting simulation showing initiation and formation a complete chip. The shades of gray show equivalent stress from low (lightest gray = 0 MPa) to high (black = 50 MPa). The simulation details are given in text of the paper. The steady-state cutting process started at $t = 4$ ms.

$\sigma_c = 40$ MPa, and $\delta_c = 0.0889$ mm. These material properties have low strain tensile modulus of $E = 1000$ MPa and are similar to properties for polyethylene. The depth of cut was 0.9 mm and the contact was frictionless. The total times for such simulations varied from about 1 hour to 4 hours depending on processor speed and number of processors used in parallel calculations. The forces initially oscillated during the ramp up phase, but once reaching constant speed, the cutting proceeded by steady state conditions. The forces reported for all simulation results are an average of the forces within the steady state region. These typical curves show stable and noise-free cutting forces. Simulations without PIC damping had similar forces, but higher noise and frequent instabilities. In other words, PIC damping stabilized the results without changing the output forces. Figure 5 shows snap shoots of the cutting process with shades of gray indicating the equivalent stress.

3. Analytical Modeling

Whether one views analytical models as a tool for verifying the simulations or vice versa, simulations were compared to existing and revised analytical models for cutting that include fracture energy in the crack propagation plane. Figure 6A defines the cutting forces. F_c and F_t are forces applied by the tool and correspond to forces measured by a tool instrumented with a biaxial force gage. The tool contacts both the chip being removed and the material below the tool resulting in normal force N and “rubbing” force F_n^b . If the contact is undergoing frictional slip by Coulomb friction, these normal forces induce shearing forces $S = \mu N$ and $F_s^b = \mu F_n^b$ where μ is the coefficient of friction. The friction law follows:

$$S = (F_c - \mu F_n^b) \sin \alpha + (F_t - F_n^b) \cos \alpha = \mu N = \mu ((F_c - \mu F_n^b) \cos \alpha - (F_t - F_n^b) \sin \alpha) \quad (11)$$

which can be rearranged and solved for F_t :

$$F_t = Z F_c + (1 - \mu Z) F_n^b \quad \text{where} \quad Z = \frac{\mu - \tan \alpha}{1 + \mu \tan \alpha} \quad (12)$$

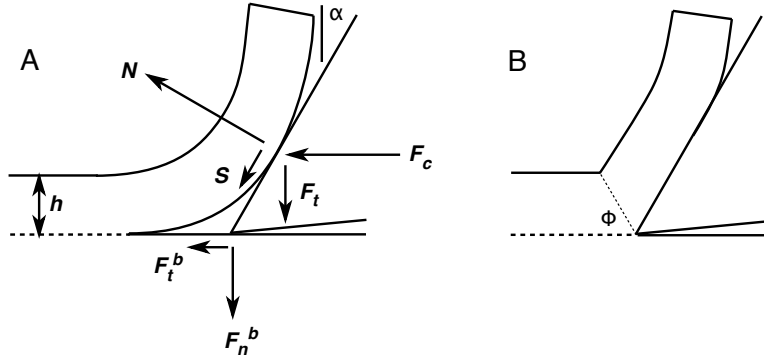


Figure 6: A. The cutting force, F_c , and transverse force, F_t , that would be measured with an instrumented tool having rake angle α . These forces can be resolved into normal forces on the cut material (N and F_n^b) and corresponding shear forces when contact has friction (S and F_t^b). The direction of all force arrows indicates a positive force in the modeling equations. B. When the tool touches the crack tip, the chip is fully plastic with a slip plane angle ϕ .

Equation (12) has several uses. In many analytical models, it is used to eliminate F_t and thereby derive a prediction for F_c alone, but this use does not eliminate F_n^b . As a consequence, many “textbook” models of cutting simply ignore the rubbing forces. This approach has two problems. First, simulations show that rubbing forces are non-negligible. Second, when F_n^b is ignored, Eq. (12) predicts that F_t is proportional to F_c , but that prediction disagrees with experiments [4, 8]. Williams *et al.* [6] noted this issue and added an adhesion term to the friction law (*i.e.*, $S = G_a + \mu N$). Although an adhesion term is easily implemented in simulations, all simulations here assumed Coulomb friction, which means prior models had to be revised to include rubbing forces before comparing to simulations. When those forces are needed in a model, Eq. (12) can be used to determine F_n^b from simulations results for F_c and F_t .

Figure 6B shows a tool touching the tip with complete yielding of the chip at slip plane angle ϕ . Atkins [1] suggests a total energy balance that accounts for fracture energy in the cutting process (which was modified here to include rubbing forces):

$$F_c dx = \tau_y \gamma (h b dx) + S \frac{\sin \phi}{\cos(\phi - \alpha)} dx + F_s^b dx + G_c b dx \quad (13)$$

where dx is an increment of crack advancement, τ_y is shear yield strength, γ is shear strain, h is cut depth, b is width, and G_c is toughness. The first term on the right is plastic work. The shear yield strength and tensile yield strength are related by $\tau_y = \sigma_y/Y$, where $Y = 2$ for Tresca yield criterion or $\sqrt{3}$ by yield criterion in Eq. (2). By geometry, the shear strain is $\gamma = \cot \phi + \tan(\phi - \alpha)$ [1]. The remaining terms are frictional work on the chip, on the rubbing surface, and fracture work, respectively. Eliminating S , F_s^b and ϕ (by minimizing cutting force [6]), the analytical model becomes:

$$\frac{F_c}{b} = G_c + \frac{\mu F_n^b}{b} + \frac{2\sigma_y h}{Y} \left(Z + \sqrt{1 + Z^2 + \frac{Y \mu G_c \sec \alpha}{h \sigma_y (\cos \alpha + \mu \sin \alpha)}} \right) \quad (14)$$

The last term in the square root differs from prior models [1, 6], but those differences are small. If contact is frictionless, the result is particularly simple (linear in h) and independent of rubbing forces:

$$\frac{F_c}{b} = G_c + \frac{2\sigma_y h}{Y} (\sec \alpha - \tan \alpha) \quad (\text{when } \mu = 0) \quad (15)$$

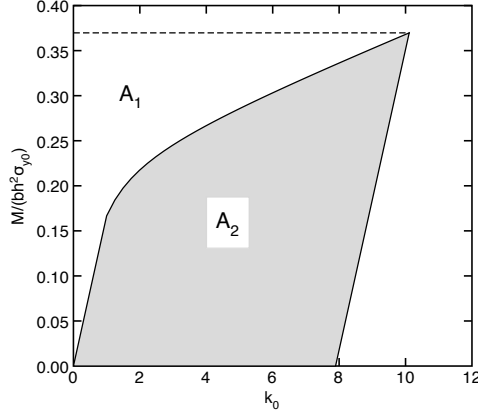


Figure 7: The curve shows moment-curvature relation for a beam with linear hardening. A_2 is the area between the loading curve and the elastic unloading curve. A_1 is the area between the applied moment (the horizontal dashed line) and the moment-curvature relation.

When the chip is not fully plastic (or is elastic), the tool will not touch the crack tip and the modeling needs a plastic bending analysis. Williams *et al.* [6] derives such an analysis resulting in:

$$\frac{F_c}{bG_c}(1 - \sin \alpha) - \frac{F_t}{bG_c} \cos \alpha = 1 + \frac{A_2(k_0)}{bG_c} \quad (16)$$

$$\frac{F_t}{bG_c} \frac{2\chi\sigma_{y0}k_0}{E'} = \frac{A_1(k_0)}{bG_c} - 1 \quad (17)$$

where $\chi = 0.64$ is a crack root rotation correction, E' is plain strain modulus, $A_1(k_0)$ and $A_2(k_0)$ are areas associated with the moment-curvature (M - κ) relation for bending the chip (see Fig. 7), and $k_0 = \kappa/\kappa_y$ where $\kappa_y = 2\sigma_{y0}/(hE')$ is the curvature at the onset of yielding. Although Williams *et al.* [6] ignores rubbing forces, they can be included by using Eq. (12) to give:

$$\frac{F_c}{bG_c} = \frac{1 + \frac{A_2(k_0)}{bG_c} + \frac{(1-\mu Z)F_n^b}{bG_c} \cos \alpha}{1 - \sin \alpha - Z \cos \alpha} \quad (18)$$

where k_0 is found by solving

$$\frac{A_1(k_0)}{bG_c} = 1 + \frac{2\chi\sigma_{y0}k_0}{E'(1 - \sin \alpha - Z \cos \alpha)} \left(Z + \frac{ZA_2(k_0)}{bG_c} + \frac{(1-\mu Z)F_n^b}{bG_c} (1 - \sin \alpha) \right) \quad (19)$$

Williams *et al.* [6] analyzes elastic-plastic materials. The analysis can be extended to hardening materials by finding areas A_1 and A_2 from moment-curvature relation for a hardening material. For the linear hardening law mentioned above, the moment curvature relation is derived to be:

$$M = \begin{cases} \frac{1}{6} bh^2 k_0 \sigma_{y0} & k_0 \leq 1 \\ \frac{1}{4} bh^2 \sigma_{y0} \left(1 - \frac{1}{3k_0^2} + \frac{E_p}{3E'} \left(1 - \frac{1}{k_0} \right)^2 (2k_0 + 1) \right) & k_0 > 1 \end{cases} \quad (20)$$

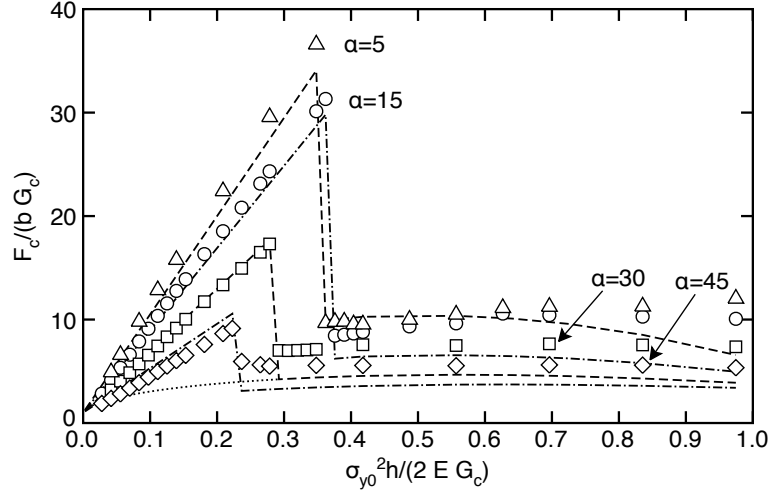


Figure 8: The simulated, dimensionless cutting forces (symbols) for an elastic-plastic plastic material with frictionless contact for various rake angles and as a function of dimensionless depth of cut. The dashed lines are analytical models for the cutting simulations.

The required areas for $k_0 \geq 1$ are:

$$\frac{A_1(k_0)}{b} = \frac{h\sigma_{y0}^2}{2E'} \left(1 - \frac{2}{3k_0} + \frac{E_p}{3E'}(k_0 - 1)^2 \left(1 + \frac{2}{k_0} \right) \right) \quad (21)$$

$$\frac{A_2(k_0)}{b} = \frac{h\sigma_{y0}^2}{2E'} \left(1 - \frac{E_p}{E'} \right) \left(1 - \frac{1}{k_0} \right)^2 \left[k_0 + \frac{1}{4} \left(1 - \frac{1}{k_0} \right) \left(\left(1 + \frac{1}{3k_0} \right) + \frac{E_p}{3E'} \left(1 - \frac{1}{k_0} \right) (2k_0 + 1)^2 \right) \right] \quad (22)$$

For $k_0 < 1$, $A_1/b = h\sigma_{y0}^2 k_0^2 / (6E')$ and $A_2 = 0$. This revised analysis reduces to Williams *et al.* [6] for both elastic ($k_0 < 1$) and plastic ($k_0 \geq 1$) bending when $F_n^b = E_p = 0$.

4. Results

The symbols in Fig. 8 show cutting force as a function of depth of cut for various rake angles and for an elastic plastic material ($E_T = 0$ and other properties same as in the ‘‘Steady State Cutting Simulations’’ section) with frictionless contact ($\mu = 0$). All plots in this paper use the scaling suggested by Williams *et al.* [6] for dimensionless forces ($F/(bG_c)$) and dimensionless depth of cut ($h\sigma_{y0}^2/(2E'G_c)$). For the properties used here, dimensionless depth of cut was $0.1392h$ or actual cuts ranged from 0.1 mm to 7 mm. At low depth of cut, the simulations linearly increased in force. At some critical depth of cut, which depended on rake angle, the cutting force dropped dramatically to a low value and thereafter varied slowly with depth of cut. The dramatic drop corresponded to a transition from the tool touching the crack tip to plastic bending with the tool removed from the crack tip and that transition occurred in a very narrow depth range. For example, Fig. 9 shows the abrupt change from touching to not touching

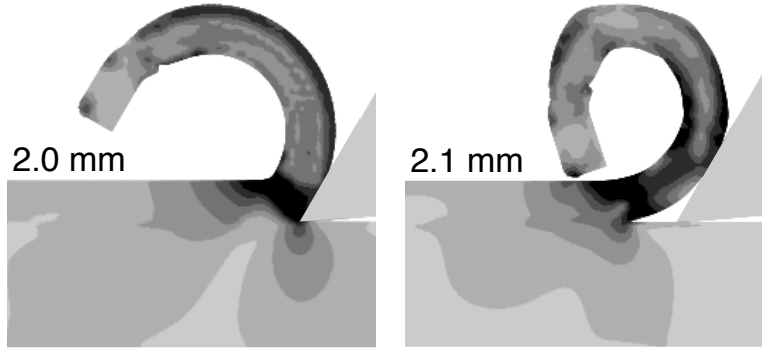


Figure 9: The tool tip/crack tip relation for an elastic-plastic material with frictionless contact for rake angle $\alpha = 30^\circ$ during steady-state cutting. The left side is for depth of cut of 2.0 mm while the right side is for 2.1 mm.

between depth of cuts 2.0 and 2.1 mm (or 0.278 and 0.292 in dimensionless units) when $\alpha = 30^\circ$. The black regions indicate plastic yielding and thus the transition corresponded to plastic collapse in the chip to incomplete yielding. Simulations with the tool touching the crack tip were challenging and needed to resolve complex contact scenarios around the crack tip. These simulations were not stable until the addition of PIC damping, but with that damping, MPM provides a good numerical tool for problems involving crack-tip contact.

The dashed lines in Fig. 8 show predictions by analytical models, but that modeling does not predict the transition from touching to plastic bending. For comparisons, the modeling curves used the crack tip touching model (Eq. (15) for $\mu = 0$) up to depth of cut where simulations showed transition to plastic bending and thereafter used the plastic bending model. The plastic bending analysis needed input of normal rubbing forces; the simulation results for this force are plotted in Fig. 10. The rubbing forces were low during tool tip touching (the increase for very thin depths of cut is discussed below), but increased rapidly just before the transition to plastic bending. In the plastic bending regime, the rubbing forces were roughly linear with depth of cut and increased significantly with rake angle. The plastic bending calculations in Fig. 8 used the linear fits to F_n^b indicated in Fig. 10. The plastic bending model has similar trends to simulations results, but does not agree as well with simulations as does the crack tip touching model.

One issue is how to predict the transition between cutting regimes? Here the transition from touching to bending was determined by simulations. One approach used in analytical modeling is to consider both models and assume the failure mode is the one with the lower force [6]. This approach disagrees with simulations. The dotted line extension for the $\alpha = 30^\circ$ simulations shows the bending model extended to lower depth of cut. At all depths of cut simulated, the minimum analytical model force is the bending model. The simulations showed, however, that for thin depths of cut, the tool reached the crack tip causing the force to be much higher than the bending model.

Figure 11 shows the effect of coefficient of friction for an elastic-plastic material ($E_T = 0$) and rake angle of $\alpha = 30^\circ$. The symbols are simulations and the dashed lines combine the touching model in Eq. (14) with a plastic bending model. The rubbing forces needed by the analytical models were taken from simulation F_n^b as a function of depth of cut. The simulations and analytical model agree well for all values of coefficient of friction for the initial region corresponding to crack tip touching. The transition to plastic bending occurred at thicker cuts when friction was added. In the plastic bending

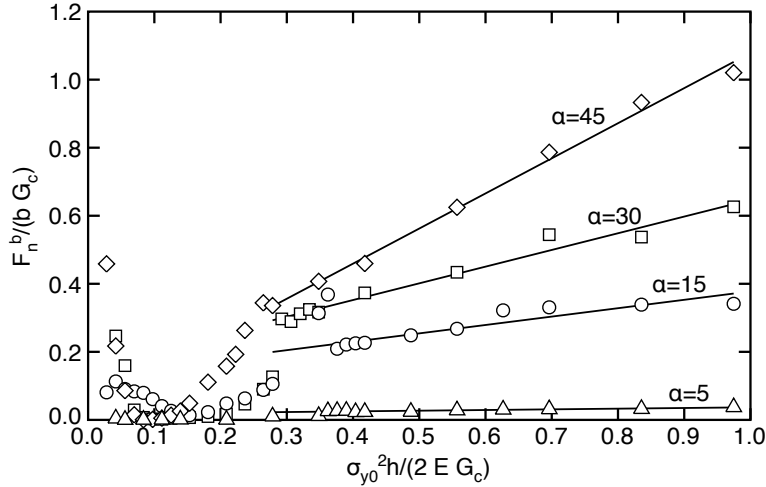


Figure 10: The simulated, dimensionless rubbing forces (symbols) for an elastic-plastic plastic material with frictionless contact for various rake angles and as a function of dimensionless depth of cut. The solid lines are linear fits to the rubbing forces for dimensionless depth of cut greater than 0.28.

regime, the models were again below the simulation results, but had similar trends for friction effects. No plastic bending mode for $\mu = 0.6$ is shown, because the analytical model does not work when $Z > 0$ or $\mu > \tan \alpha = 0.577$. In dynamic frictional sliding, the tangential stress is $S = \min(S_0, \mu N)$ where S_0 is shear force corresponding to stick conditions and μN is shear force during sliding. The simulations can combine slip and stick frictional contact while the analytical model assumes S is always μN , and thus only applies during complete frictional sliding.

All simulations with an elastic-plastic material showed a large and rapid transition from tool tip touching to plastic bending regime, but no such transitions are seen in experiments on real materials [4, 8]. Either the simulations are unrealistic or an elastic-plastic material does not represent real materials well. To test for the later hypothesis, simulations were run for frictionless contact at a rake angle of $\alpha = 30^\circ$ as a function of the hardening modulus, E_T ; the results are in Fig. 12. Increasing E_T shifted the transition to lower depth of cut and significantly reduced the magnitude of the transition. By the time E_T reached 25 MPa, which is only 2.5% of the elastic modulus of $E = 1000$ MPa, the force drop at the transition was nearly gone. Realistic modeling for cutting of most materials will need to account for hardening properties of those materials.

When $E_T = 100$ MPa, all simulations were in the plastic bending regime. Figure 13 compares simulations (symbols) to plastic bending theory (dashed lines) for $E_T = 100$ MPa, frictionless contact, and various rake angles. The rubbing forces needed as input for the plastic bending theory, were found from simulations results. The simulations and bending theory have similar trends. The cutting force increased as the rake angle decreased and it increased rapidly for thin cuts, but then leveled off for deeper cuts. The differences are that the simulation forces are 10% to 90% higher than the bending model and simulation forces continued to rise while the model predicts a maximum in force followed by a decrease for deep cuts. Although either the simulation or the bending model may be wrong, an alternative explanation is that they are both correct but are solving different problems. The analytical modeling was based on small-strain, one-dimensional, elasticity theory and crack growth used fracture

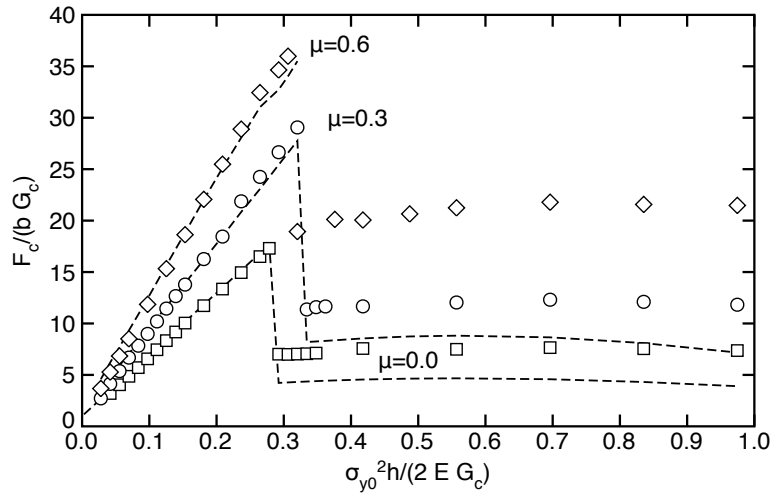


Figure 11: The simulated, dimensionless cutting forces (symbols) for an elastic-plastic material as a function of the coefficient of friction for rake angle $\alpha = 30^\circ$ and as a function of dimensionless depth of cut. The dashed lines are analytical models for the cutting simulations.

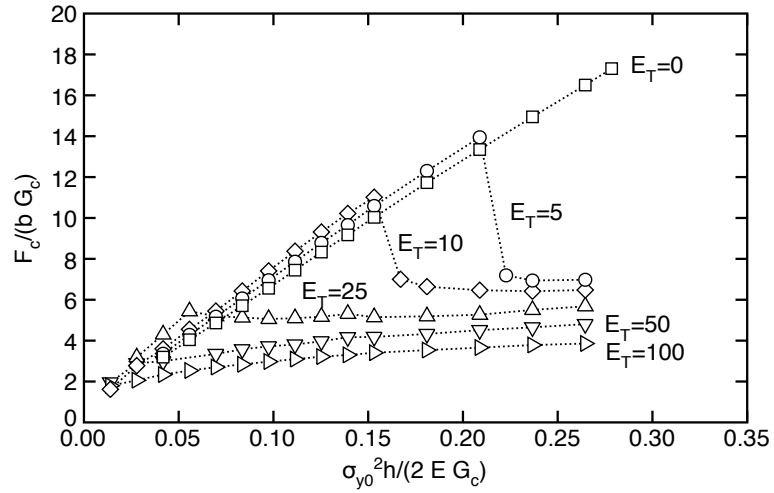


Figure 12: The simulated, dimensionless cutting forces (symbols) for a linear hardening material as a function tangent modulus (E_T) for rake angle $\alpha = 30^\circ$ and as a function of dimensionless depth of cut. The dotted lines connect the points and are not analytical modeling results.

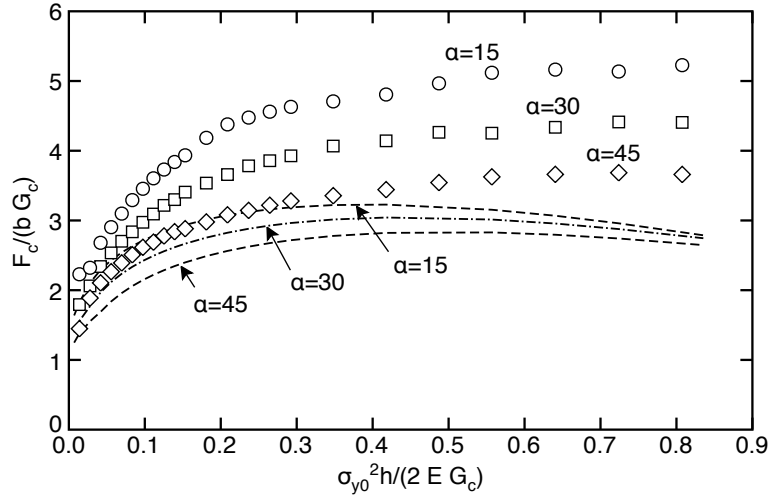


Figure 13: The simulated, dimensionless cutting forces (symbols) for a linear hardening material with $E_T = 100$ MPa for various rake angles and as a function of dimensionless depth of cut. The dashed lines are analytical models for the cutting simulations.

mechanics with a fixed value of G_c . The simulations used large-strain, two-dimensional plasticity theory and crack growth used a cohesive law with a fixed value of G_c but potentially variable cohesive stress (σ_c) or shape of the law (other than cubic). Because simulation shear strains reached 80%, one should expect differences between small-strain and large-strain material models. Perhaps the force peak in the analytical model is an artifact of small-strain assumptions? A similar peak was never seen in simulations even when carried out to very deep cuts. The 10% to 90% difference in magnitudes may be due to fracture modeling. Figure 14 shows simulations compared to modeling for $E_T = 100$ MPa, frictionless contact, rake angle $\alpha = 30^\circ$, fracture toughness $G_c = 2000$ J/m², but with different values for the cohesive stress. The simulation results were above or below models by changing the cohesive stress. Additional simulations looked at varying the cohesive law from a cubic law to a triangular law and also showed differences in magnitude and curvature of the results. Clearly, it would be possible vary the cohesive stress and shape of the cohesive law to achieve an exact match between theory and modeling.

Figure 15 shows the effect of cohesive stress on simulations and modeling for both touching and plastic bending; these simulations repeated the simulations in Fig. 11, but changed cohesive stress from $\sigma_c = 40$ MPa to $\sigma_c = 10$ MPa. The lower cohesive stress improved the agreement in the plastic bending regime and retained the good agreement of the touching regime. A significant affect of cohesive stress is that it reduced the thickness need to convert to plastic bending. In summary, simulation results were sensitive to cohesive law details.

Although failure was always simulated as occurring at a constant total J_c , the output did provide the mode mixity at failure. Figure 16 plots scatter diagram of mode I percent for all elastic plastic simulations in Figs. (8) and (11) as a function of Z , which was a good indicator of mode mixity. The solid symbols are for all results in the plastic bending regime, where failure modes were always more than 90% mode I and independent of Z . The spread of the symbols was caused by slow decrease in mode I character as the depth of cut increased. The open symbols are for touching mode and they were correlated with Z . Increasing Z by either decreasing rake angle or increasing friction both caused similar decreases in mode I character. The mode I character was also affected by the cohesive stress.

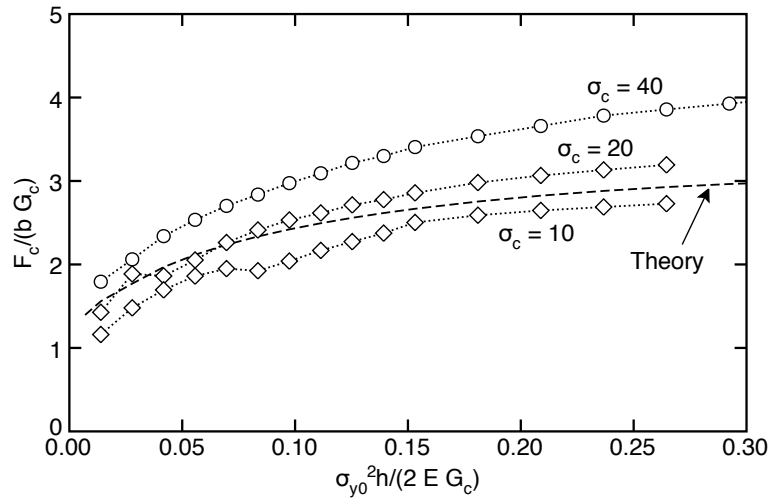


Figure 14: The simulated, dimensionless cutting forces (symbols) for a linear hardening material with $E_T = 100$ MPa a function of the cohesive stress (σ_c) for rake angle $\alpha = 30^\circ$ and as a function of dimensionless depth of cut. The dashed line is the analytical model for the cutting simulations.

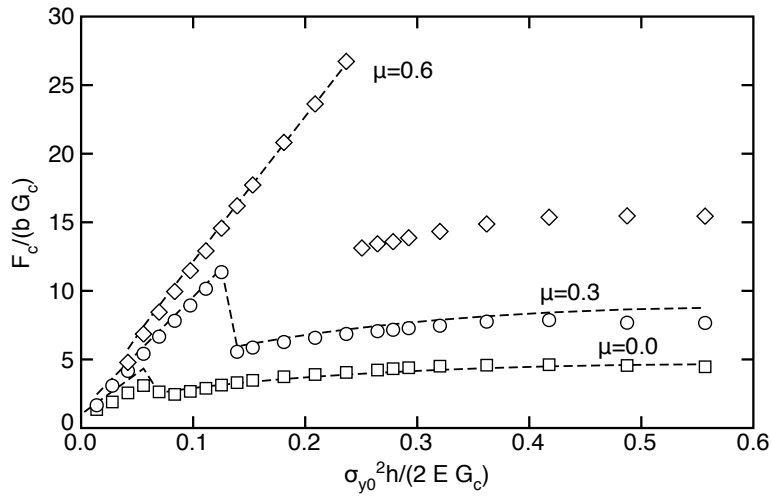


Figure 15: The simulated, dimensionless cutting forces (symbols) for an elastic-plastic plastic material with cohesive stress $\sigma_c = 10$ MPa as a function of the coefficient of friction for rake angle $\alpha = 30^\circ$ and as a function of dimensionless depth of cut. The dashed lines are analytical models for the cutting simulations

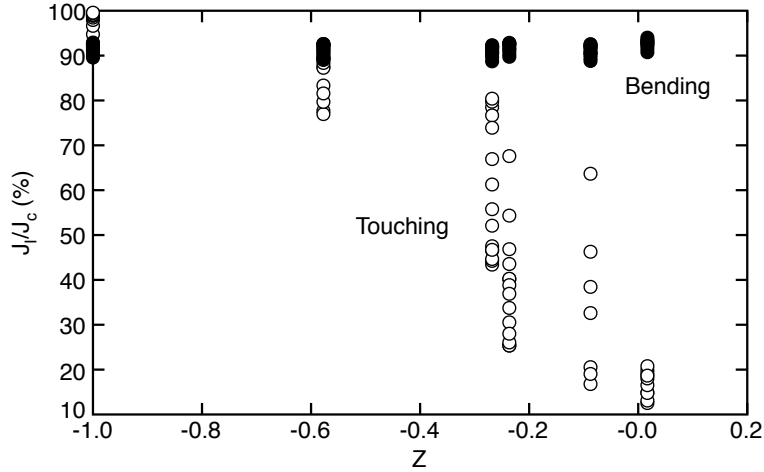


Figure 16: The fraction mode I content in the released energy during steady state cutting as a function of Z . The filled symbols are for simulations in the plastic bending regime. The open symbols are for simulations with the tool touching the crack tip.

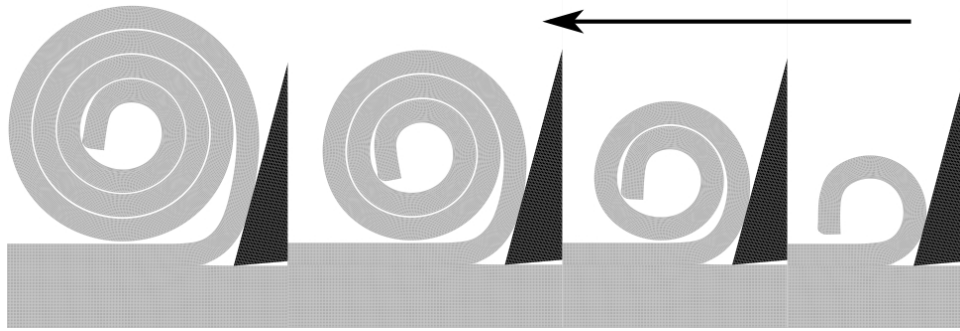


Figure 17: Snapshots of a long-time cutting simulations for depth of cut 0.5 mm, rake angle $\alpha = 15^\circ$, and hardening materials with $E_T = 100$ MPa. The arrow indicates the direction of cut.

As σ_c decreased from 40 MPa to 10 MPa, the mode I character of the plastic bending regime decreased from over 90% to about 75%.

A goal of these simulations was to model steady-state cutting including chip curling, when it occurs. Figure 17 show a long-time simulation in the plastic bending regime ($E_T = 100$ MPa) for rake angle $\alpha = 15^\circ$ and depth of cut of 0.5 mm. The simulations modeled chip curling well. The modeling of chip curling requires dynamic modeling of self contact as the chip curves over and reaches the material surface. Fortunately, MPM automatically models self contact, but this “free” contact modeling can only model stick contact conditions. The modeling of frictional sliding, as done between tool and the cut material, uses different multimaterial methods that are capable of modeling friction sliding. For this specific problem, self contact by stick is sufficient because as their chip curls, there should be little relative motion between the layers of the chip.

The simulations described here were robust and able to vary many parameters, thus providing potential for many future applications. Two challenges for future work are simulating very thin cuts

and simulating tool sharpness effects. All successful simulations here were for depths of cut 0.1 mm or higher. Because experiments extend to thinner cuts [4, 8], it would be useful to simulate that regime. The increase in rubbing forces for thin cuts (see Fig. 10) may be onset of an artifact that causes instability. One possibility for the instability may be the cohesive law methods. The cohesive law used had a critical opening displacement of $\delta_c = 0.0889$ mm, which is similar in magnitude to the thinnest cuts possible. Perhaps alternative fracture mechanics methods are needed to simulate very thin cuts? Modeling of tool sharpness requires changing the discretization of the tool and enough particles to resolve the radius of curvature at the tool tip. Setting up such a simulation is easy, but the first simulation attempts did not work well. The main issue is likely finding accurate normals around the tool tip. With a sharp tip, the normals could be exactly specified, but with a blunt tip, they need to be calculated within the simulation. Perhaps modeling of tool sharpness effects requires further improvements in MPM contact methods?

5. Conclusions

This paper shows that the material point method (MPM) is capable of robust simulations of orthogonal cutting that include extensive amounts of tool advance such that the simulations reach steady-state cutting processes with chip formation and curling. The development of stable MPM simulations required some important MPM changes. The most important features were high-strain material models, accurate modeling of tool shape and its contact normals, and the use of PIC damping. The simulations modeled tool advance by ductile fracture mechanics with a cohesive zone along the crack propagation path. Although cohesive zone laws are common in numerical modeling of crack propagation, they may not provide a fundamental fracture mechanics analysis. Cohesive zones were used here because they helped control propagation and not because they were judged the best way to model crack propagation. The simulation results showed that some results (*i.e.*, plastic bending regime) are sensitive to the shape of the cohesive law even when total toughness is constant. All numerical modeling should precede with caution when interpreting results that rely on cohesive laws. Despite concerns over use of cohesive laws, the MPM simulations provide a robust tool for studying new cutting problems that are beyond the capabilities of analytical models. Two examples are veneer peeling of logs and planing of wood. These problems require new material models and accounting for complex geometries in the tool set ups.

Acknowledgement

This material is based upon work supported by the National Institute of Food and Agriculture, United States Department of Agriculture, under McIntire-Stennis account #229862, project #OREZ-WSE-849-U.

References

- [1] A. Atkins, Modelling metal cutting using modern ductile fracture mechanics: Quantitative explanations for some longstanding problems, *International Journal of Mechanical Sciences* 45 (2) (2003) 373 – 396.
- [2] A. Atkins, Rosenhain and Sturney revisited: The 'tear' chip in cutting interpreted in terms of modern ductile fracture mechanics, *Proceedings of the Institution of Mechanical Engineers, Part C: Journal of Mechanical Engineering Science* 218 (10) (2004) 1181–1194.

- [3] A. Atkins, Toughness and cutting: A new way of simultaneously determining ductile fracture toughness and strength, *Engineering Fracture Mechanics* 72 (6) (2005) 849–860.
- [4] Y. Patel, B. Blackman, J. Williams, Determining fracture toughness from cutting tests on polymers, *Engineering Fracture Mechanics* 76 (18) (2009) 2711 – 2730.
- [5] D. J. Wyeth, A. G. Atkins, Mixed mode fracture toughness as a separation parameter when cutting polymers, *Eng. Fract. Mech.* 76 (18) (2009) 2690–2697.
- [6] J. G. Williams, Y. Patel, B. R. K. Blackman, A fracture mechanics analysis of cutting and machining, *Engineering Fracture Mechanics* 77 (2) (2010) 293–308.
- [7] J. G. Williams, The fracture mechanics of surface layer removal, *Int. J. Fract.* 170 (2011) 37–48.
- [8] K. Semrick, Determining fracture toughness by orthogonal cutting of polyethylene and wood-polyethylene composites, Master's thesis, Oregon State University (2012).
- [9] T. D. Marusich, M. Ortiz, Modelling and simulation of high speed machining, *International Journal for Numerical Methods in Engineering* 38 (1995) 3675–3694.
- [10] D. Sulsky, Z. Chen, H. L. Schreyer, A particle method for history-dependent materials, *Comput. Methods Appl. Mech. Engrg.* 118 (1994) 179–186.
- [11] S. G. Bardenhagen, E. M. Kober, The generalized interpolation material point method, *Computer Modeling in Engineering & Sciences* 5 (2004) 477–496.
- [12] S. G. Bardenhagen, J. E. Guilkey, K. M. Roessig, J. U. Brackbill, W. M. Witzel, J. C. Foster, An improved contact algorithm for the material point method and application to stress propagation in granular material, *Computer Modeling in Engineering & Sciences* 2 (2001) 509–522.
- [13] J. A. Nairn, Modeling of imperfect interfaces in the material point method using multimaterial methods, *Computer Modeling in Eng. & Sci.* 92 (3) (2013) 271–299.
- [14] J. A. Nairn, Material point method calculations with explicit cracks, *Computer Modeling in Engineering & Sciences* 4 (2003) 649–664.
- [15] J. A. Nairn, Analytical and numerical modeling of R curves for cracks with bridging zones, *Int. J. Fract.* 155 (2009) 167–181.
- [16] Y. E. Aimene, J. A. Nairn, Simulation of transverse wood compression using a large-deformation, hyperelastic-plastic material model, *Wood Science and Technology in press*, 2014. doi:10.1007/s00226-014-0676-6.
- [17] J. C. Simo, T. J. R. Hughes, *Computational Inelasticity*, Springer, New York, 1998.
- [18] A. Needleman, A continuum model for void nucleation by inclusion debonding, *J. Appl. Mech.* 54 (1987) 525–531.
- [19] Q. D. Yang, M. D. Thouless, Mixed-mode fracture analysis of plastically-deforming adhesive joints, *International Journal of Fracture* 110 (2) (2001) 175–187.

- [20] A. Sadeghirad, R. M. Brannon, J. Burghardt, A convected particle domain interpolation technique to extend applicability of the material point method for problems involving massive deformations, *Int. J. Num. Meth. Engng.* 86 (12) (2011) 1435–1456.
- [21] V. Lemiale, A. Hurmane, J. A. Nairn, Material point method simulation of equal channel angular pressing involving large plastic strain and contact through sharp corners, *Computer Modeling in Eng. & Sci.* 70 (1) (2010) 41–66.
- [22] J. Brackbill, D. Kothe, H. Ruppel, FLIP: A low-dissipation, particle-in-cell method for fluid flow, *Computer Physics Communications* 48 (1) (1988) 25 – 38.
- [23] F. H. Harlow, The particle-in-cell method for numerical solution of problems in fluid dynamics, *Methods in Computational Physics* 3 (1964) 319—343.
- [24] A. Stomakhin, C. Schroeder, L. Chai, J. Teran, A. Selle, A material point method for snow simulation, *ACM Trans. Graph.* 32 (4) (2013) 102:1–102:10. doi:10.1145/2461912.2461948.
- [25] J. A. Nairn, Material point method (NairnMPM) and finite element analysis (NairnFEA) open-source software, <http://code.google.com/p/nairn-mpm-fea/> (2014).
- [26] G. Ayton, A. M. Smondyrev, S. G. Bardenhagen, P. McMurtry, G. A. Voth, Interfacing molecular dynamics and macro-scale simulations for lipid bilayer vesicles, *Biophys J* 83 (2002) 1026–1038.
- [27] D. J. Evans, B. L. Holian, The Nose-Hoover thermostat, *J. Chem. Phys.* 83 (1985) 4069—4074.
- [28] L. Shen, Z. Chen, A silent boundary scheme with the material point method for dynamic analyses, *Computer Modeling in Engineering & Sciences* 7 (3) (2005) 305–320.